J Solid State Electrochem (2009) 13:1831–1847
DOI 10.1007/s10008-008-0745-6

ORIGINAL PAPER

Oxide density distribution across the barrier layer during the steady state growth of porous anodic alumina films: chronopotentiometry, kinetics of mass and thickness evolution and a high field ionic migration model

G. Patermarakis · H. Karayianni · K. Masavetas · J. Chandrinos

Received: 18 February 2008 / Revised: 11 November 2008 / Accepted: 12 November 2008 / Published online: 9 December 2008

Abstract The steady state growth of porous anodic alumina films in oxalate solutions at various conditions was studied by chronopotentiometry, mass balance and optical microscopy methods enabling determination of consumed Al, film mass and thickness, current efficiencies, Al^{3+} and O^{2-} transport numbers across barrier layer, etc. The film thickness growth rate was found to be proportional to O^{2-} anionic current. A high field ionic migration model was developed. It predicted that, during anodising, the local oxide density across barrier layer rises from 2.6 in Al|oxide to 4.59–5.22 g cm^{-3} in oxide|electrolyte interface with mean value ≈3.21–3.52 g cm^{-3}. The field strength rises from the first to second interface. The mechanism of Al oxidation near the Al|oxide interface embraces the transformation of the Al lattice to a transient, rare oxide one sustained by field with comparable Al^{3+} spacing parameter. The oxide near the Al|oxide interface and around the density maximum in the oxide|electrolyte interface are under different levels of electro-restriction stresses. During relaxation, the oxide behaves like a solid-fluid material suppressing the initial density distribution.

Keywords Porous anodic alumina · Growth mechanism · Oxide density spectrum · Fluidity · Al to oxide lattice transformation

G. Patermarakis (✉) · H. Karayianni · K. Masavetas · J. Chandrinos
School of Chemical Engineering, Department of Materials Science and Engineering, National Technical University, Iroon Polytechniou 9, Zografou, 157 80 Athens, Greece
e-mail: gpaterma@central.ntua.gr

Nomenclature

a_2 and a_3	activation (half-jump) distance of O^{2-} and Al^{3+} migrations inside the barrier layer.
	$b = N_{2,m} d_c^{-2/3}$
	$b' = a_2 d_c^{1/3}$
B	$n_2 b' F_c / RT$
C_a and C_s	concentration of $H_2C_2O_4$ and of $Al_2(C_2O_4)_3$ or $Na_2C_2O_4$ in the bath bulk electrolyte solution
COR_1, COR_2 and COR_3	correlation coefficient derived by regression analysis of P vs. Δt, h vs. t and k' vs. jt_{an} plots
d_c, $d_{c,o\|e}$, $d_{c,m\|o}$ and $d_{c,a}$	local density of oxide across the barrier layer, this density near the o|e and m|o interfaces and the average density of oxide across the barrier layer
D	diameter of the hemispherical section surface across the barrier layer
D_b	pore base diameter
D_c	cell width
ΔV	anodising voltage
Δt	$t - t_m$
Δm	$m - m(t_m)$
E, $E_{o\|e}$, $E_{m\|o}$ and E_a	local field strength across the barrier layer, this strength near the o|e and m|o interfaces and the average field strength across the barrier layer

F_c	Faraday's constant
h	total thickness of anodic film
h_0	intersection of the linear h vs. t plots
j	current density
k	rate constant of oxide production resulting from Faraday's law (1.76097×10^{-4} g C^{-1})
k'	rate of porous film thickness growth or the inclination of the linear h vs. t plots;
k_1 and k_2	dissociation constants of $H_2C_2O_4$
m	mass of oxide film spread over the whole geometric surface area of Al specimens S_g during anodising
m|o	metal|oxide interface
n	surface density of pores in the (quasi)steady state stage
n_2 and n_3	valence of O^{2-} and Al^{3+} ions
N	Avogadro constant
$N_{2,m}$ and $N_{3,m}$	surface concentration of mobile O^{2-} and Al^{3+} ions within the barrier layer
ν_2 and ν_3	vibration frequency of O^{2-} and Al^{3+} ions or the number of chances per second the ions may jump the energy barrier (activation energy) if they have sufficient energy
o|e	oxide|electrolyte interface
$P=(\Delta m/\Delta t)(kjS_g)^{-1}$	dimensionless factor directly related to O^{2-} transport number ($=t_{an}+z_1(\Delta t)+z_2(\Delta t)^2$)
R	universal gas constant
S_g	geometric surface area of Al specimens (30.75 cm^2)
$S=2^{-1}\pi nD^2$, $S_b=2^{-1}\pi nD_b^2$ and $S_c=2^{-1}\pi nD_c^2$	hemispherical section surface area across the barrier layer per square centimetre of S_g and this surface near the o|e and m|o interfaces
t	anodising time
t_m	anodising time where ΔV becomes minimum and the (quasi)steady state growth of porous layer starts
t_{an} and t_{ca}	transport numbers of O^{2-} and Al^{3+}
T	temperature
W_2 and W_3	activation energy for the migration of O^{2-} and Al^{3+} ions within the oxide (<0)
z	gradient of the linear k' vs. jt_{an} plot
z_1 and z_2	parameters depending on all anodising conditions and electrolyte kind and composition (<0), derived by fitting the equation $P=t_{an}+z_1(\Delta t)+z_2(\Delta t)^2$ to the experimental results P vs. Δt

Introduction

Porous anodic alumina films form by Al anodising in oxalic, chromic, phosphoric, sulphuric (and other sulphate), malonic, tartaric, citric, etc. acid solutions. The pore forming anodising of Al is characterised, e.g. for sulphuric and oxalic acid electrolytes, by a transient stage where a flat barrier layer forms on the surface of which pores are later nucleated towards its end [1–4], followed by another transient stage where pores are developed and organised yielding the characteristic structure of these films [5] that is finally followed by a steady state one. The steady state structure of films is characterised as a close-packed array of approximately hexagonal, columnar cells, each of which contains an elongated, roughly cylindrical pore normal to the surface extending between the film's external surface and the Al_2O_3|Al interface where it is sealed by a thin, compact, hemispherical shell-shaped barrier type oxide layer with thickness roughly around 1 nm/V of applied voltage [6–8]. The structure of films is defined by the surface density of pores, usually of the order 10^{10}–10^{11} cm^{-2}; base diameter of pores, of the order of a few up to several tens of nanometres; shape and ordering degree of pores which depend on the kind of electrolyte and conditions of the anodic oxidation of Al [7–10]. The oxide, examined after anodising, is an almost anhydrous amorphous (or nanocrystalline) γ or γ'-Al_2O_3 material [7, 8, 11]. Protons and electrolyte anions are embodied in small amounts variable across the barrier layer and pore walls depending on electrolyte kind and conditions [4, 7–9, 11]. Anions exist in a pore surface layer leaving an anion almost free layer near the metal and cell boundaries [4, 9].

Due to their peculiar nanometer-scale porous structure, physicochemical properties and strong adherence to the Al metal surface, the porous anodic alumina films are important materials finding numerous applications such as protection, decoration and improvement of mechanical properties of Al, magnetic memories, catalysis, nuclear reactors, rechargeable batteries, as templates for synthesising emitters, fuels cells, in nanoscience–nanotechnology, etc. [5, 12, 13].

The structure and nature/composition of films, after anodising, have been extensively examined by scanning electron microscopy (SEM), transmission electron microscopy (TEM), atomic force microscopy (AFM) and many other methods of solid-state analysis [2, 9, 14–21]. These methods as well as other ones like XR microanalysis, IR, ESR, electro- and photo-luminescence, etc. for porous films [2, 4, 22–25] and implanted marker atoms, secondary ion mass spectroscopy, glow optical emission discharge spectroscopy, etc. [15, 26–28] for barrier type films were employed, also after anodising, to examine the distribution of various species and their transport numbers, oxide inhomogeneity, etc. Thus, TEM [18–21], AFM [20] and

chemical dissolution [20, 21] revealed circular voids of the order of 10 nm along three cell junctions lines and long narrow holes crack-like voids crossing pore walls emerging from underlying metal ridges in phosphoric acid and other electrolytes porous films, voids in three cell junctions of barrier type oxide on preconditioned Al [18, 19], voids in anion-free layer of barrier type films [20] and variable space charge and allied electronic defects in barrier layer of phosphoric acid porous films [21]. Voids were absent or much rarer in the barrier layer bulk of such porous films and were entirely absent in oxalic and sulphuric acid porous films [18].

In these and numerous other publications, studies on the mechanism of oxide growth during the previous three stages, kinetic studies and studies aiming at modelling in the steady state the distributions of potential and current across the barrier layer [29] and the combined stress field-driven ionic transport and material flow in ordered porous films [30] are met. The structure, nature/composition and density of oxide after anodising are generally assumed to be identical with that during anodising. Despite the large amount of published work, a generally adopted integrated theory elucidating the mechanisms of pore generation, self-organising of cells/pores, steady state growth of porous layer, invariance of geometry around the barrier layer during steady state and effect of conditions on porous structure is still absent. To our knowledge, inhomogeneity related to the change or not of local density of compact barrier layer of porous films during their growth, the mechanism of transformation of Al metal lattice to that of anodic oxide (whatever can be meant as lattice for this amorphous or nanocrystalline material after anodising) and any probable change of oxide lattice after the cease of field application and film relaxation during and after anodising, impossible to be derived by direct in situ experimental methods, have not been discussed up to now.

In this study, along the lines of previous work [5], focussing on the steady state, by treatment of physical, structural, kinetic and potentiometric results by a suitably developed model and method, the distribution of oxide density across the barrier layer and the mechanism of Al transformation to oxide during the film growth are studied. The state of oxide lattice during film growth and its change after oxide relaxation are also discussed. These are of great importance for the solid-state electrochemistry of Al anodising, interpretations of peculiar properties of films and their applications.

Experimental

In view of the fact that films grown in oxalate solutions are relatively pure materials with small amounts of electrolyte anions embodied in pore walls [9, 28] and usually with hexagonally well-organised pores [31], oxalate electrolytes were used. Al anodising was performed in vigorously stirred oxalate solutions, $H_2C_2O_4$+$Al_2(C_2O_4)_3$ or $Na_2C_2O_4$, at different C_a's and C_s's ($C_a>0$, $C_s\geq 0$), so that the anodising electrolytes had different kinds and concentrations of cations, H^+, Al^{3+} (more specifically related complex anions and other species—see below) and Na^+ (not participating in forming other complex species), and anions, $C_2O_4^{-2}$ and $HC_2O_4^-$ (dissociation constants of $H_2C_2O_4$ $k_1=6.5\times10^{-2}$ and $k_2=6.1\times10^{-5}$ [32]) and pH's (Table 1) and at different T's, 20–40 °C (±0.1–0.2 °C), j's, 5–25 mA cm^{-2}, and t's, up to 120 min. The above different composition electrolytes were used among others to elucidate any probable, even slight, effect of anions and/or cations of electrolyte on transport numbers and related charge transport mechanism. The results in Table 1 show that the addition of $Na_2C_2O_4$ raises pH. This is explained by the effect of $C_2O_4^{2-}$, coming from dissociation of $Na_2C_2O_4\rightarrow 2Na^+ + C_2O_4^{2-}$, on the equilibrium processes:

$$H_2C_2O_4 + H_2O \rightleftarrows H_3O^+ + HC_2O_4^- \quad (1)$$

$$HC_2O_4^- + H_2O \rightleftarrows H_3O^+ + C_2O_4^{2-} \quad (2)$$

raising pH. However, $Al_2(C_2O_4)_3$ appreciably lowers pH explained by that Al^{3+} in non-alkaline solution, as in this case, exist as hydrated species $Al(OH_2)_6^{3+}$, which subsequently undergo hydrolysis [33, 34]:

$$Al(OH_2)_6^{3+} + H_2O \rightleftarrows Al(OH_2)_5(OH)^{2+} + H_3O^+ \text{(first stage)}, \quad (3)$$

$$Al(OH_2)_5OH^{2+} + H_2O \rightleftarrows Al(OH_2)_4(OH)_2^+ + H_3O^+ \text{(second stage)}, \quad (4)$$

$$Al(OH_2)_4OH^+ + H_2O \rightleftarrows Al(OH_2)_3(OH)_3 + H_3O^+ \text{(third stage)}. \quad (5)$$

Also, along with the monomer ions, $Al(OH)^{2+}$ and $Al(OH)_2^+$, the polymers, $Al_2(OH)_2^{4+}$ and $Al_3(OH)_6^{3+}$, exist. More complex ions like $Al[(OH)_5Al_2]_n^{(n+3)+}$ and $Al_6(OH)_{15}^{3+}$ may also exist. The H^+ thus formed are many more than those consumed by processes 1 and 2 shifted to the left, so that pH is reduced; pure aluminium salts like, $Al_2(SO_4)_3$, indeed yield sufficiently acidic solutions where porous Al anodising effectively takes place [35]. Due to the above processes, some significant amount of salt anions $C_2O_4^{2-}$ is transformed to $H_2C_2O_4^-$ and $H_2C_2O_4$. The pure

Table 1 Regression analysis parameters of plots P vs. Δt (Fig. 3) and h vs. t ($t \geq t_m$; Fig. 5) for different anodising oxalate electrolytes having different pH's, temperatures (T) and current densities (j)

Electrolyte	pH	T (°C)	j (mA cm^{-2})	t_{an}	z_1 (min^{-1})	Z_2 (min^{-2})	COR_1	k' (μm min^{-1})	h_0 (μm)	COR_2
0.5 M $H_2C_2O_4$	0.728	25	15	0.730	−0.00014	≈0	0.9651	0.451	−0.1375	0.9999
1 M $H_2C_2O_4$	0.521	25	15	0.733	−0.00028	≈0	0.9984	0.45	−0.0030	0.9999
0.5 M $H_2C_2O_4$+0.25 M $Al_2(C_2O_4)_3$	0.322	25	5	0.667	−0.00045	≈0	0.8988	0.126	−0.3655	0.9976
0.5 M $H_2C_2O_4$+0.25 M $Al_2(C_2O_4)_3$	0.322	25	15	0.736	−0.00023	≈0	0.9736	0.445	0.0024	0.9999
0.5 M $H_2C_2O_4$+0.25 M $Al_2(C_2O_4)_3$	0.322	25	25	0.753	−0.00008	≈0	0.3930	0.756	0.1514	0.9995
0.5 M $H_2C_2O_4$+0.25 M $Al_2(C_2O_4)_3$	0.433	20	15	0.759	−0.00015	≈0	0.9500	0.446	−0.1448	0.9997
0.5 M $H_2C_2O_4$+0.25 M $Al_2(C_2O_4)_3$	0.432	30	15	0.720	−0.00043	≈0	0.9803	0.435	−0.2146	0.9996
0.5 M $H_2C_2O_4$+0.25 M $Al_2(C_2O_4)_3$	0.413	40	15	0.656	−0.00076	-5.695×10^{-6}	0.9984	0.409	−0.0428	0.9999
0.5 M $H_2C_2O_4$+0.5 M $Al_2(C_2O_4)_3$	0.293	25	15	0.739	−0.00020	≈0	0.9672	0.451	−0.3367	0.9999
0.5 M $H_2C_2O_4$+0.1 M $Na_2C_2O_4$	0.857	25	15	0.749	−0.00029	≈0	0.9943	0.448	−0.0787	0.9999

Linear or second-order polynomial regression for the P vs. Δt and linear for the h vs. t plots

acid electrolytes have H_3O^+ and $HC_2O_4^-$ as predominant cations and anions whilst the mixture electrolytes have Al^{3+} and related species, or Na^+, as predominant cations and $C_2O_4^{2-}$ as predominant anions at concentrations of oxalate salts comparable to those used in this study (see also later).

Al sheets with thickness 0.3 mm and purity ≥99.95% (Merck—pro analysi) were used. The shape and dimensions of the two-face Al anodes and Pb cathodes used, the whole anodising procedure and the procedure for washing and neutralising Al anodes after anodising to remove the pore filling solution and contained compounds and drying were described elsewhere [10]. The maximum t employed was smaller enough than that at which in each condition the average maximum pore diameter approaches first the average cell width and the surface aspect starts to change from shiny transparent and similar to Al metal to a mat, milky one [10, 36], thus assuring strict as possible conditions of model application.

The film mass was determined by a suitable mass balance method [36], by accuracy 10^{-4} g. The cross-section thickness of films was determined at the centre of Al specimens in suitable metallographic specimens [10] by optical microscopy with an error ≤0.5%. Vigorous stirring and conditions eliminating parasitic phenomena, like pitting and burning [37, 38], as described in this study, assure uniform thickness along the Al surface with changes within the experimental error [39]. The film mass and thickness are necessarily involved in the ensuing high field model and the accuracy of their determination defines at most the validity of model application.

Al anodising was followed chronopotentiometrically. The anodic potential (e.g. vs. SHE) almost coincides with the potential drop from the o|e to the m|o interface [40, 41] and is close to (strictly speaking slightly lower than) the anodising voltage [40]. For ease, the latter was recorded up to ≈85 V. Chronopotentiometric curves are used, among others, to define the start time of steady state film growth, t_m, beyond which the characteristic structure of porous films has been established, as revealed by SEM of film surface and imprints of film on the metal surface after oxide removal [5].

Since a basic admittance for the applicability of model under consideration is the obeisance of consumed Al to Faraday's law, this should be checked for the electrolytes and all conditions employed. For this purpose, at each anodising condition and electrolyte composition, the mass of consumed Al was determined at three times: at a time near t_m of the start of steady state, at the maximum employed one and at an intermediate one. For finding the masses of consumed Al, the masses of specimens before anodising and after anodising and removing the oxide layer by chromophosphoric acid solution [7, 8, 10] were measured, the difference of which yielded the mass of consumed Al.

From accumulated heretofore results, there is no indication for any detectable reduction or increase of the thickness of the barrier layer and of the lateral scalloped barrier layer that becomes pore wall material, after opening the circuit and relaxing of oxide lattice/bulk. Thus, use of potentiometric results during anodising and of suitable physical properties and structural features of films found after anodising to describe the steady state growth of barrier layer during anodising is allowable.

Results

Chronopotentiometric study: determination of the start time of steady state stage

The ΔV vs. t plots appear in Fig. 1a–c. Three successive stages appear: (1) The step 0A of abrupt almost linear rise of ΔV, corresponding to the initial transient stage of flat barrier layer growth in the last range of which the porous structure is nucleated [1–4]; it was short enough, of the

order of 10 s, and thus it is not easily discerned in Fig. 1; however, its detailed separate presentation is unnecessary as there is interest for the steady state (BC). (2) The step AB of the subsequent drop of ΔV within a t of the order of 1 min, clearly seen, is the second transient stage where the pore/cell system units develop and cover gradually all the surface and are self-organised to a more regular ordering within each metal grain surface or in the whole surface [5, 14–17, 42–45], the proper almost final number of cells/pores is set up and a steady state pore base diameter, nature/composition of barrier layer and electrolyte composition in pores is finally achieved. (3) The last stage BC where ΔV remains constant (steady state) or changes (increases) with t (quasi-steady state). The characteristic max and min ΔV's and related t's generally depend on the anodising conditions. The ΔV at $t=t_m$, marking the start of steady state, increases with increasing j and decreasing T and decreases with both C_a and C_s. Their dependence on conditions and electrolyte composition are related to the two former transient stages where the proper steady state n, D_c and D_b is established the discussion of which, however, escapes the scope of this study.

The potential drop and processes from Al to electrolyte ($\approx\Delta V$) are divided into those in the oxide and in the m|o and o|e interfaces; those in o|e interface have been investigated earlier [5, 41, 46]. For thick barrier layer, as in steady state, the potential drops in interfaces are tiny compared to that in oxide [29, 41] and the change of ΔV with t, T, j and electrolyte composition reflects the effect of its thickness and nature/composition (which are, in turn, affected also by T, j and probably partially by electrolyte composition) and of T and j per se on ΔV.

Current efficiency for Al oxidation

For each pair of employed T and j, electrolyte composition and the three aforementioned times, defined from Fig. 1, the Al consumption was close enough to the mass anticipated by Faraday's law within a range of error at maximum ±0.15%. Thus, the ionic current across the barrier layer is practically close to 100% of current and the electronic current related to galvanoluminescence during anodising [47] and oxygen evolution is tiny irrespective of the j, T, t and ΔV employed. The basic admittance of model application for Al consumption according to Faraday's law is thus fully satisfied.

Determination of the O^{2-} transport number in the steady state

The cation and anion transport numbers across the barrier layer are kinetic parameters necessarily involved in the research of various aspects of the whole mechanism of film

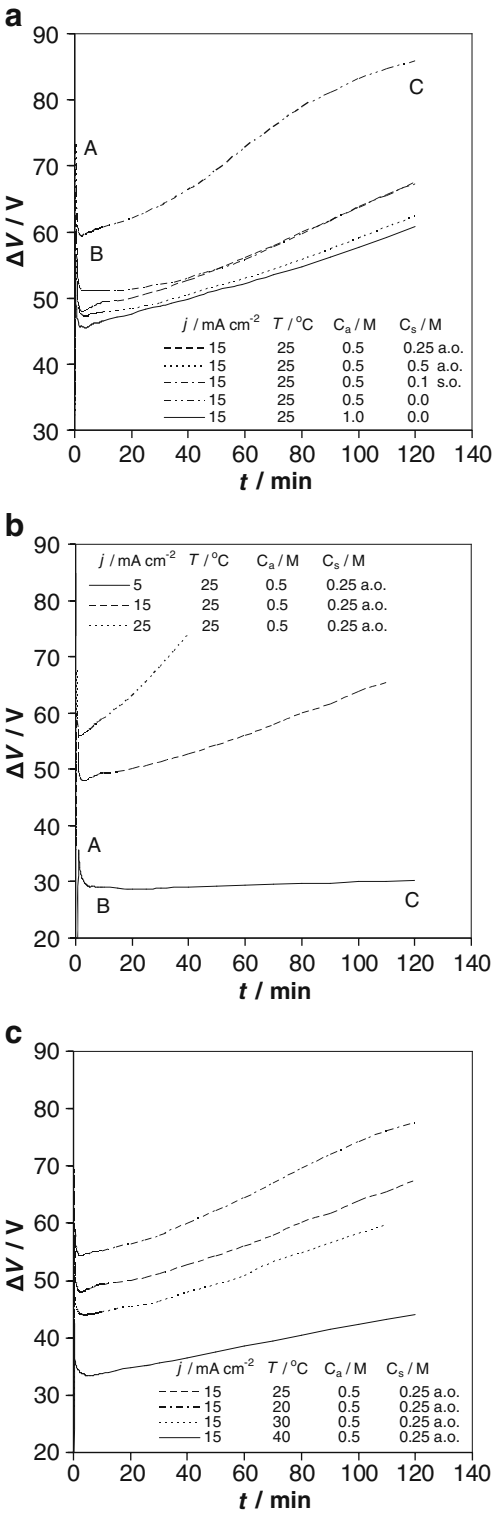

Fig. 1 Plots of ΔV vs. t at different T's, j's, C_a's and C_s's showing the effect of **a** composition of mixture electrolyte $H_2C_2O_4$+$Al_2(C_2O_4)_3$ or $Na_2C_2O_4$, i.e. of C_a and C_s at constant current, j, and temperature, T, and of **b** current density, j, and **c** temperature, T, for constant mixture composition, C_a and C_s. *a.o.* aluminium oxalate, *s.o.* sodium oxalate

growth. Recently [5], a convenient and reliable method to determine these transport numbers supplied with a suitable model was introduced. The model combines macroscopic parameters like film mass, the rate of porous film thickness growth, the real surfaces of charge exchange in the m|o and o|e interfaces, nanostructure parameters, transport numbers of Al^{3+} and O^{2-} and other elementary atomic–ionic scale kinetic and thermodynamic parameters. The model in its first founded form, embracing all elementary parameters to assist comprehension of its physical meaning, is summarised by the equations:

$$P = (\Delta m/\Delta t)\left(kjS_g\right)^{-1} = t_{an} + z_1(\Delta t) + z_2(\Delta t)^2, (z_1 \text{ and } z_2 \le 0) \quad (or\ t_{an} = \lim\ P \text{ when } \Delta t = t - t_m \to 0), \tag{6}$$

$$kjt_{an} = k' d_{c,a}\left(1 - 4^{-1}\pi n D_b^2\right), \tag{7}$$

$$jt_{an}S_c^{-1} = N_{2,m}\nu_2 n_2 F_c N^{-1} \exp[(W_2 N + n_2 a_2 F_c E)/(RT)], \tag{8}$$

$$jt_{ca}S_c^{-1} = N_{3,m}\nu_3 n_3 F_c N^{-1} \exp[(W_3 N + n_3 a_3 F_c E)/(RT)], \tag{9}$$

$$\begin{aligned}\ln\left[\left(jS_c^{-1}\right)^{[1/(n_2a_2)]-[1/(n_3a_3)]}\right] &= \ln\left[(1-t_{ca})^{-[1/(n_2a_2)]}t_{ca}^{[1/(n_3a_3)]}\right] \\ &+ \ln\left[\left(N_{2,m}\nu_2 n_2 F_c N^{-1}\right)^{[1/(n_2a_2)]}\left(N_{3,m}\nu_3 n_3 F_c N^{-1}\right)^{-[1/(n_3a_3)]}\right] \\ &+ [W_2/(n_2a_2) - W_3/(n_3a_3)]N/(RT)\end{aligned} \tag{10}$$

where the high field Eq. 10 is derived by suitable fusion of the high field Eqs. 8 and 9. Since $|W_2|$ and $|W_3|$ are generally 0.5–1 eV [48], E is generally roughly 1–1.5 V nm^{-1} [6–8] and a_2 and a_3 are around 0.1 nm [37] then $(W_2N + n_2a_2F_cE)/(RT)$ and $(W_3N + n_3a_3F_cE)/(RT) << 0$. The formulation of the model was based on the experimentally verified consumption of Al according to Faraday's law, e.g. for H_2SO_4 and $H_2C_2O_4$ electrolytes films and conditions employed [5, 10, 35], equivalent to practically solely ionic current through the barrier layer and O^{2-} and Al^{3+} mobile species in the region adjacent to the m|o interface where pure oxide forms by O^{2-} reaching there [9, 18, 28, 49–52] and where only traces of electrolyte anions can exist; the migrating Al^{3+} are field ejected to pore base filling solution, without forming oxide in the o|e interface region unlike the case of barrier type films. The ejected Al^{3+} ions react with H_2O according to processes $Al^{3+}+6H_2O \leftrightarrows Al(OH_2)_6^{3+}$ followed by processes 3, 4 and 5 [33, 34] and with electrolyte anions to form aluminium oxalate which, in dense enough solutions, is condensed to colloidal aluminium oxalate precipitate [39]. In steady state, t_{an} also expresses current efficiency for oxide formation. A direct and convenient estimate of t_{an} is thus possible from the P vs. Δt plots by regression analysis. Other methods of t_{an} determination, e.g. those usually applied in barrier type films and based on determining the thickening of oxide layer below and above a level of implanted marker atoms [28], imply a rather uniform oxide composition, density or other parameters, across the film, etc. during the film growth which may be unsecured (see later). However, the developed method does not imply any such adoption. A probable tiny effect of traces of electrolyte anions incorporated in the deeper oxide layer near the m|o interface is discussed later.

The m vs. t and P vs. Δt plots are shown in Figs. 2 and 3; in agreement to Eq. 1, P is a declining function of Δt. The $|z_2|$ was found to be tiny ≈0, and the linear model satisfactorily applies, for all cases besides that at T=40 °C where z_2 acquires nonzero value since the rate of pore wall dissolution reaction involved in it [5], becomes accordingly appreciable at this higher temperature. The t_{an}, z_1, z_2 and COR_1 are given in Table 1. The COR_1 is high, tending to 1, besides only one case at the higher j due to the necessary narrow range of t's employed and not to experimental inaccuracy. Table 1 shows that t_{an} and t_{ca}=1−t_{an} depend mostly on T and j, and t_{an} (t_{ca}) decreases (increases) with T and increases (decreases) with j and faintly, but systematically, vary with electrolyte concentration. They also faintly vary with the kind of salt whilst the effect of $Na_2C_2O_4$, added in much smaller concentration than $Al_2(C_2O_4)_3$, is larger than that of $Al_2(C_2O_4)_3$. The t_{an} and t_{ca} thus found meet literature values [22, 53, 54] roughly 0.6–0.75 and 0.4–0.25, respectively.

Though the effect of electrolyte composition on t_{an} is trivial, the elucidation of its origin can yield much

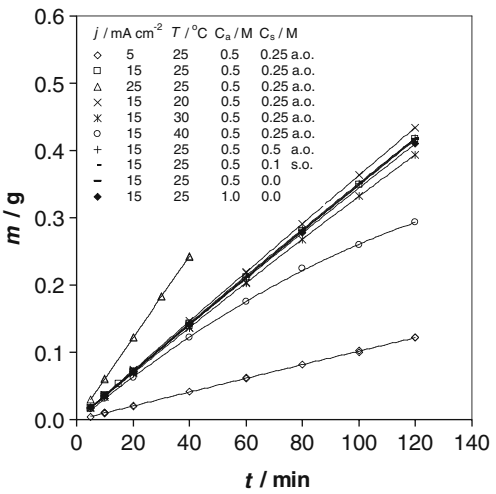

Fig. 2 Plots of m vs. t at different T's, j's, C_a's and C_s's. *a.o.* aluminium oxalate, *s.o.* sodium oxalate

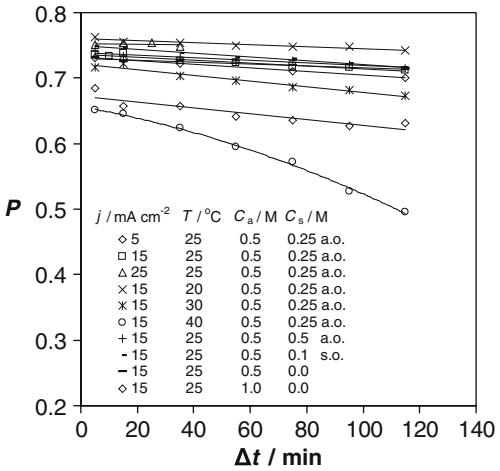

Fig. 3 Plots of dimensionless factor $P=(\Delta m/\Delta t)(kjS_g)^{-1}$ vs. Δt at different T's, j's, C_a's and C_s's. *a.o.* aluminium oxalate, *s.o.* sodium oxalate

important information. Since the drop of pH with C_s of $Al_2(C_2O_4)_3$ causes a rise of t_{an} whilst the rise of pH with C_s of $Na_2C_2O_4$ also causes a rise of t_{an}, it seems that pH or H^+ concentration (or activity) per se do not exert any detectable influence on t_{an}. In the case of $Al_2(C_2O_4)_3$, the drop of pH and the concomitant rise of H^+ concentration (or activity) is attended by a rise of concentrations of cationic species related to Al^{3+}, processes 3, 4 and 5. On the other hand, the rise of pH (and the concomitant drop of H^+ concentration or activity) is attended by a rise of Na^+ concentration in the case of $Na_2C_2O_4$. Thus, the kind and also the concentration of other cations like Al^{3+} and related species, or Na^+, do not exert any detectable influence on t_{an}. The observed tiny change of t_{an} with electrolyte composition thus must be attributed solely to electrolyte anions. For pure acid electrolyte at C_a=0.5 M, j=15 mA cm^{-2} and T=20, 30 and 40 °C, the t_{an} are 0.780, 0.710 and 0.664, at C_a=0.5 M, T=25 °C and j=5 and 25 mA cm^{-2}, the t_{an} are 0.664 and 0.707 and at C_a=1.5 M, T=25 °C and j=15 mA cm^{-2}, the t_{an} is 0.742 [5]. These results also conform to the above described systematic trends of t_{an} variation with T, j and C_a and thus also to the effect of electrolyte anions.

The slight effect of electrolyte anions on t_{an} must be attributed apparently to those embodied in the barrier layer. The field in solution near the o|e interface, depending on conditions, is relatively high as lying necessarily between the very high field in the oxide of the order of ≈10^7 V cm^{-1} [7, 8] and low field in pore filling solution (e.g. of the order of 0.37 V cm^{-1} for sulphuric acid films [40]) where thus only $C_2O_4^{2-}$ exist. Their concentrations in solution and interface and the amount of embodied anions vary similarly when the other parameters of Al anodising remain constant. The $C_2O_4^{2-}$ exist at concentrations of some orders of magnitudes higher in the mixed electrolytes than in pure acid ones. For example, considering the case of pure acid with C_a=0.5 M, the concentrations of $HC_2O_4^-$ and $C_2O_4^{2-}$ estimated from k_1 and k_2 are roughly ≈0.13 and ≈3.3×10^{-3} M, whilst for the mixed electrolytes, the $C_2O_4^{2-}$ concentration approaches that predicted by the added salt, i.e. of the order of ≈0.1 M and above. The stronger effect of $Na_2C_2O_4$ on t_{an} than that of $Al_2(C_2O_4)_3$ is explained by the fact that, in the case of $Al_2(C_2O_4)_3$, a significant amount of $C_2O_4^{2-}$ is transformed to $H_2C_2O_4^-$ and $H_2C_2O_4$, processes 1, 2, 3, 4 and 5, thus $C_2O_4^{2-}$ in solution must remain at lower concentration for all C_s's employed than for $Na_2C_2O_4$. The mechanism by which the embodied anions slightly affect t_{an} is outlined in the following.

Comparison of ΔV_m (Fig. 1) with t_{an} (Table 1) at various conditions shows that a rough general tendency of ΔV_m and t_{an} to rise together is observed, which, however, is not a strict, monotonic one. Thus, Fig. 1 shows cases where ΔV_m's in the start of steady state differ appreciably but the t_{an}'s almost coincide and vice versa. The determined t_{an}'s undoubtedly characterise the start of steady state, Eq. 6. However, a query arises from the fact that ΔV rises with t, more as j increases and T decreases, in the (quasi)steady state which could be perhaps associated with some change of mechanism details related to transport numbers. But detailed data available for sulphuric acid films (Patermarakis et al., under preparation) on a related subject show almost coincidence of t_{an}'s at corresponding conditions where, however, the ΔV in steady state is generally several times smaller than that for oxalate baths. For example, for sulphuric acid films at C_a=1.5 M, T=25 °C and j=15 mA cm^{-2}, t_{an}=0. 736 whilst ΔV_m=14.5 V, whilst for oxalic acid at similar conditions, t_{an}=0.742 and ΔV_m=42 V [5]. Hence, the rise of ΔV with t during the steady state cannot be associated with a detectable change of t_{an}.

Distribution of oxide density across the barrier layer during the steady state film growth

Representative cross-section micrographs of films appear in Fig. 4 where the uniformity of oxide layer thickness is shown for two, unlike enough, cases conditions and the reliability of film thickness measurements is thus assured. The h vs. t ($\geq t_m$) plots are given in Fig. 5. Accurate linear dependences are observed with inclinations k', intersections h_0 and COR_2's given in Table 1. The k' increases with j, slightly decreases with T and is faintly affected by the concentration of electrolyte anions. The decrease of film thickness due to oxide chemical dissolution by the electrolyte is negligible at each condition (of the order of 0.1 nm min^{-1} [10, 55] or less) and thus the above k' values virtually characterise the actual rates of h rise.

The plot of k' vs. jt_{an} (Fig. 6) is an accurate straight line with gradient z=6.767×10^{-5} cm^3 C^{-1}, intercept

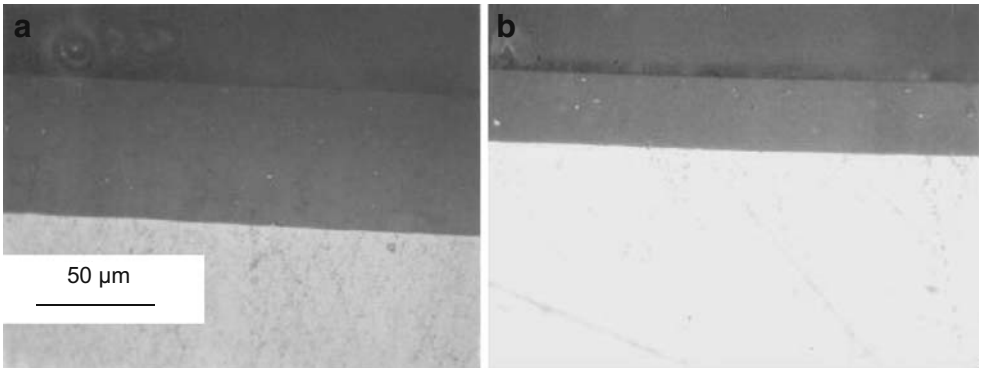

Fig. 4 Optical microscopy photomicrographs of the cross-sections of films (magnification ×500) at C_a=0.5 M (**a** and **b**), C_s=0.25 M (aluminium oxalate; **a**) and 0.1 M (sodium oxalate; **b**), j=15 mA cm^{-2} (**a** and **b**), T= 20 °C (**a**) and 25 °C (**b**) and t= 120 min (**a**) and 60 min (**b**)

0.006034 μm min^{-1} or 1.00567 10^{-8} cm s^{-1} ≈0 and COR_3= 0.9992. A similar straight line was also found for sulphuric acid films essentially coinciding with the above (Patermarakis et al., under preparation), e.g. with inclination 6.983× 10^{-3} cm^3 C^{-1}, intercept ≈0 and COR_3=0.9983. Since oxide forms exclusively in the m|o interface, or in a thin oxide layer just adjacent to this interface [41], each member of Eq. 7 must also equal the rate of oxide growth in the space just adjacent to the m|o interface per square centimetre of S_g that is $k'd_{c,m|o}=zjt_{an}d_{c,m|o}$. It must also equal the rate of oxide production according to Faraday's law and current density j minus the rate of electrochemical degradation of oxide in the pore base surface region that is $kj - k'4^{-1}\pi nD_b^2 d_{c,o|e}$. Hence, Eq. 7 becomes:

$$kjt_{an} = k'd_{c,a}\left(1 - 4^{-1}\pi nD_b^2\right) = k'd_{c,m|o} = kj - k'4^{-1}\pi nD_b^2 d_{c,o|e} \quad (11)$$

or

$$kjt_{an} = zjt_{an}d_{c,a}\left(1 - 4^{-1}\pi nD_b^2\right) = zjt_{an}d_{c,m|o} = kj - zjt_{an}4^{-1}\pi nD_b^2 d_{c,o|e} \quad (12)$$

or

$$d_{c,a}\left(1 - 4^{-1}\pi nD_b^2\right) = d_{c,m|o} = k/z = 2.6023\ \mathrm{g\ cm^{-3}} = d_{c,m|o}t_{an}^{-1} - d_{c,o|e}4^{-1}\pi nD_b^2, \quad (13)$$

from which,

$$d_{c,o|e}^{-1} = t_{an}(1 - t_{an})^{-1}\left(d_{c,m|o}^{-1} - d_{c,a}^{-1}\right). \quad (14)$$

Since $d_{c,m|o}^{-1} - d_{c,a}^{-1} > 0$, then always $d_{c,a} > d_{c,m|o}$. The Eq. 14 can also take the form:

$$d_{c,o|e}^{-1} - d_{c,a}^{-1} = t_{an}(1 - t_{an})^{-1}\left(d_{c,m|o}^{-1} - d_{c,a}^{-1}\right) - d_{c,a}^{-1} = (1 - t_{an})^{-1}\left(t_{an}d_{c,m|o}^{-1} - d_{c,a}^{-1}\right). \quad (15)$$

For the amorphous oxide material, the $N_{2,m}$ and a_2 have the meaning of the average values for all different planes and directions and ought to be proportional to $d_c^{2/3}$ and $d_c^{-1/3}$ (thus $N_{2,m} = bd_c^{2/3}$ and $a_2 = b'd_c^{-1/3}$). For each equipotential hemispherical surface across the barrier layer, Eq. 8 becomes:

$$jt_{an}S^{-1} = bd_c^{2/3}\nu_2 n_2 F_c N^{-1}\exp\left[\left(W_2N + n_2b'd_c^{-1/3}F_cE\right)\Big/(RT)\right]. \quad (16)$$

Since $W_2N + n_2b'd_c^{-1/3}F_cE << 0$, the variation of d_c in the relatively narrow range from $d_{c,m|o}$ to the highest possible (see below, Table 2) affects the exponential factor less than the pre-exponential one and d_c, like $jt_{an}S^{-1}$, must vary monotonically. Near m|o and o|e interfaces, Eq. 16 becomes:

$$jt_{an}\left(2^{-1}\pi nD_c^2\right)^{-1} = bd_{c,m|o}^{2/3}\nu_2 n_2 F_c N^{-1}\exp\left[\left(W_2N + n_2b'd_{c,m|o}^{-1/3}F_cE_{m|o}\right)\Big/(RT)\right], \quad (17)$$

$$jt_{an}\left(2^{-1}\pi nD_b^2\right)^{-1} = bd_{c,o|e}^{2/3}\nu_2 n_2 F_c N^{-1}\exp\left[\left(W_2N + n_2b'd_{c,o|e}^{-1/3}F_cE_{o|e}\right)\Big/(RT)\right], \quad (18)$$

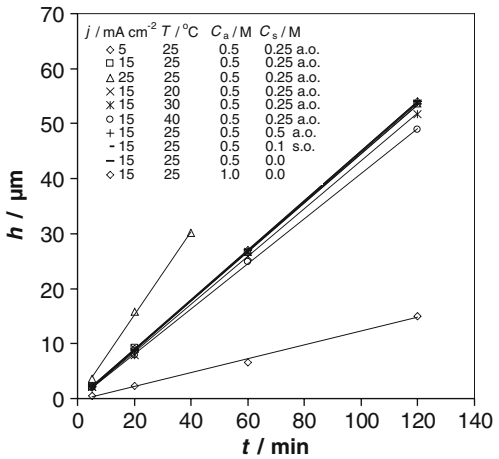

Fig. 5 Plots of h vs. t at different T's, j's, C_a's and C_s's. *a.o.* aluminium oxalate, *s.o.* sodium oxalate

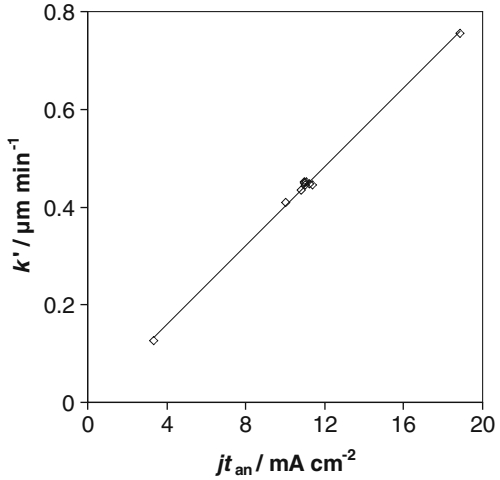

Fig. 6 Plot of k' vs. jt_{an} for all the anodising conditions and electrolyte compositions employed

from which:

$$\begin{aligned} D_c^{-2}D_b^2 &= \left(nD_c^2\right)^{-1}nD_b^2 \\ &= d_{c,m|o}^{2/3}d_{c,o|e}^{-2/3}\exp\left[\left(d_{c,m|o}^{-1/3}E_{m|o}-d_{c,o|e}^{-1/3}E_{o|e}\right)n_2b'F_c\right)\Big/(RT)\Big] \\ &= d_{c,m|o}^{2/3}d_{c,o|e}^{-2/3}\exp\left[\left(d_{c,m|o}^{-1/3}E_{m|o}-d_{c,o|e}^{-1/3}E_{o|e}\right)B\Big/(RT)\right] \end{aligned} \tag{19}$$

where $nD_c^2 = 4/3$, [41], and generally:

$$\begin{aligned} D_c^{-2}D^2 &= \left(nD_c^2\right)^{-1}nD^2 \\ &= d_{c,m|o}^{2/3}d_c^{-2/3}\exp\left[\left(d_{c,m|o}^{-1/3}E_{m|o}-d_c^{-1/3}E\right)n_2b'F_c\right)\Big/(RT)\Big] \\ &= d_{c,m|o}^{2/3}d_c^{-2/3}\exp\left[\left(d_{c,m|o}^{-1/3}E_{m|o}-d_c^{-1/3}E\right)B\Big/(RT)\right] \end{aligned} \tag{20}$$

where $B=n_2b'F_c/(RT)$.

The potential was considered heretofore varying linearly across the barrier layer which means that E remains constant [29, 41]. Here, this confinement is relaxed and E is generally considered variable. Due to barrier layer geometry, E would be assumed to vary proportionally to the true j, $j(2^{-1}\pi nD^2)^{-1}$, and therefore, strongly across the barrier layer. Combination of Eqs. 19 and 20 for cancelling B and taking into account this dependence of E on nD^2 gives:

$$\begin{aligned} &\left[d_{c,m|o}^{-1/3}-d_{c,o|e}^{-1/3}\left(nD_c^2/nD_b^2\right)\right]\ln\left[\left(nD_c^2\right)^{-1}nD^2\left(d_{c,m|o}^{-2/3}d_c^{2/3}\right)\right] \\ &\quad-\left[d_{c,m|o}^{-1/3}-d_c^{-1/3}\left(nD_c^2/nD^2\right)\right] \\ &\quad\ln\left[\left(nD_c^2\right)^{-1}nD_b^2\left(d_{c,m|o}^{-2/3}d_{c,o|e}^{2/3}\right)\right]=0. \end{aligned} \tag{21}$$

Following steps 2–8 of the method developed below to solve the system of Eqs. 13, 23 (or 21) and 26, it was found that the system embracing Eq. 21 has no solution, showing that this case is unreal, without physical meaning. That dependence of E on nD^2 implies a rather uniform nature/composition and d_c of barrier layer justifying the inexistence of solution. Hence, a slight variation of E is expected, also verified by the ensuing results, which allows considering a linear variation of E or:

$$\begin{aligned} E &= E_{m|o}+\left(E_{o|e}-E_{m|o}\right)(D_c-D_b)^{-1}(D_c-D) \\ &= E_{m|o}\left[1+\left(E_{o|e}E_{m|o}^{-1}-1\right)\left(n^{1/2}D_c-n^{1/2}D_b\right)^{-1}\left(n^{1/2}D_c-n^{1/2}D\right)\right]. \end{aligned} \tag{22}$$

After cancelling B from Eqs. 19 and 20 and combining Eq. 22, then:

$$\begin{aligned} &\left(d_{c,m|o}^{-1/3}-d_{c,o|e}^{-1/3}E_{o|e}E_{m|o}^{-1}\right)\ln\left[\left(nD_c^2\right)^{-1}\left(nD^2\right)\left(d_{c,m|o}^{-2/3}d_c^{2/3}\right)\right] \\ &-\left\{d_{c,m|o}^{-1/3}-d_c^{-1/3}\left[1+\left(E_{o|e}E_{m|o}^{-1}-1\right)\left(n^{1/2}D_c-n^{1/2}D_b\right)^{-1}\left(n^{1/2}D_c-n^{1/2}D\right)\right]\right\} \\ &\quad\ln\left[\left(nD_c^2\right)^{-1}\left(nD_b^2\right)\left(d_{c,m|o}^{-2/3}d_{c,o|e}^{2/3}\right)\right]=0. \end{aligned} \tag{23}$$

which embraces the ratio $E_{o|e}/E_{m|o}$. For uniform E across the barrier layer ($E_{o|e}=E_{m|o}=E$), it becomes:

$$\begin{aligned} &\left(d_{c,m|o}^{-1/3}-d_{c,o|e}^{-1/3}\right)\ln\left[\left(nD_c^2\right)^{-1}\left(nD^2\right)\left(d_{c,m|o}^{-2/3}d_c^{2/3}\right)\right] \\ &-\left(d_{c,m|o}^{-1/3}-d_c^{-1/3}\right)\ln\left[\left(nD_c^2\right)^{-1}\left(nD_b^2\right)\left(d_{c,m|o}^{-2/3}d_{c,o|e}^{2/3}\right)\right]=0. \end{aligned} \tag{24}$$

In the vicinity of each equipotential hemispherical surface across the barrier layer with area $S=4^{-1}\pi nD^2$ ($D_b\le D\le D_c$) per square centimetre of S_g, the oxide density is d_c. Then, the average $d_{c,a}$ of oxide contained in the corresponding volume of barrier layer $12^{-1}\pi n\left(D_c^3-D_b^3\right)$ (Fig. 7) can be calculated from:

$$\begin{aligned} d_{c,a} &= \left[12^{-1}\pi n\left(D_c^3-D_b^3\right)\right]^{-1}\int_{D_b}^{D_c}2^{-1}\pi nD^2d_c\,d(D/2) \\ &= \left[12^{-1}\pi n\left(D_c^3-D_b^3\right)\right]^{-1}n^{-1/2}\int_{n^{1/2}D_b}^{n^{1/2}D_c}4^{-1}\pi\left(n^{1/2}D\right)^2d_c\,d\left(n^{1/2}D\right). \end{aligned} \tag{25}$$

Table 2 Values of the proper $E_{o|e}E_{m|o}^{-1}$ yielding acceptable solution and of the parameters $d_{c,o|e}$, $d_{c,a}$ and nD_b^2 derived from the solution of Eqs. 13, 23 and 26 at various t_{an}'s

t_{an}	Proper $E_{o\|e}E_{m\|o}^{-1}$	$d_{c,o\|e}$ (g cm^{-3})	$d_{c,a}$ (g cm^{-3})	nD_b^2
0.656	111.75/88.25	5.22	3.52	0.33
0.700	110/90	4.8	3.39	0.30
0.730	109.5/90.5	4.59	3.29	0.27
0.742	109.25/90.75	4.5	3.26	0.26
0.759	108.5/91.5	4.36	3.21	0.24

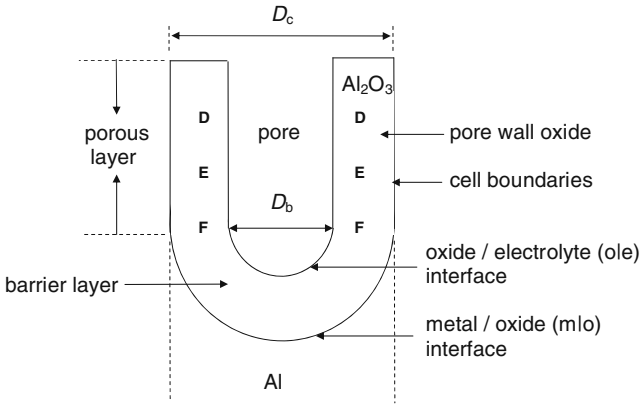

Fig. 7 Section parallel to pore axis of a columnar cell of porous anodic alumina film during anodising with different structural details

Given the $E_{o|e}E_{m|o}^{-1}$ value, Eqs. 13, 23 and 25 constitute a system solvable by numerical analysis. The next step by step method was followed:

1. An $E_{o|e}E_{m|o}^{-1}$ value is inserted, like $(100+x)/(100-x)$ where x is a small number compared to 100, showing directly the percent rise and decrease of E in the o|e and m|o interfaces with respect to the mean E value in the middle of barrier layer, e.g. 100/100=1, 105/95=1.105, etc., starting from the first.
2. For each $E_{o|e}E_{m|o}^{-1}$, different values for $d_{c,o|e}$ are tried, like 3, 3.01, 3.02, …, etc. up to 5.60 g cm^{-3}.
3. From each such $d_{c,o|e}$ value, $d_{c,m|o}$=2.6023 g cm^{-3} and Eq. 13, $d_{c,a}$ and nD_b^2 are calculated.
4. The region from $n^{1/2}D_b$ to $(4/3)^{1/2}$ is divided into a large number i of small equal finite differential paces so that i+1 discrete values $(n^{1/2}D)_{i=0-i}$ are determined.
5. The corresponding $d_{c,i}$ values are then found from Eq. 23.
6. Numerical integration of Eq. 25 that gives:

$$\begin{aligned} d_{c,a} &= \left[12^{-1}\pi n\left(D_c^3 - D_b^3\right)\right]^{-1} n^{-1/2}\sum_{i=0}^{i} 12^{-1}\pi n^{3/2}\left(D_{i+1}^3 - D_i^3\right)d_{c,i} \\ &= \left[12^{-1}\pi\left[\left(nD_c^2\right)^{3/2} - \left(nD_b^2\right)^{3/2}\right]\right]^{-1} \\ &\quad \sum_{i=0}^{i} 12^{-1}\pi\left(n^{3/2}D_{i+1}^3 - n^{3/2}D_i^3\right)d_{c,i} \\ &= \left\{12^{-1}\pi\left[\left(nD_c^2\right)^{3/2} - \left(nD_b^2\right)^{3/2}\right]\right\}^{-1} \\ &\quad \sum_{i=0}^{i} 12^{-1}\pi\left[\left(n^{1/2}D_{i+1}\right)^3 - \left(n^{1/2}D_i\right)^3\right]d_{c,i}. \end{aligned} \tag{26}$$

7. Successive trying of steps 2–6 until the $d_{c,a}$ of step 6 converges with $d_{c,a}$ of step 3 at least up to their third decimal figures. The last circle solution is considered the acceptable one.
8. Repetition of steps 1–7 starting from a next $E_{o|e}E_{m|o}^{-1}$ value.

Though for $E_{o|e}/E_{m|o} \geq 1$ solution exists, confirming the reality of the case, no solution exists for $E_{o|e}E_{m|o}^{-1} < 1$ or, the same, this case in unreal, having no physical meaning.

The basic starting parameters involved in this method are $d_{c,m|o}$ and t_{an}, both of which are known. Five characteristic cases are examined, covering all the range of t_{an}'s determined, that of the highest t_{an}=0.759, that of the lowest t_{an}=0.656 and an intermediate one t_{an}=0.730, corresponding to results met in Table 1, and two arbitrary intermediate cases (not met in Table 1) of t_{an}=0.700 and 0.742, the second of which is also met below. The solution plots of d_c vs. $n^{1/2}D\left(n^{1/2}D_b \leq n^{1/2}D \leq n^{1/2}D_c = (4/3)^{1/2}\right)$ are shown in Fig. 8a–e. For all t_{an}'s and $E_{o|e}E_{m|o}^{-1} = 1$, an intensive peak appears. The d_c peak values are always roughly about two times the density of γ-Al_2O_3 (≈4 g cm^{-3} [56]), the structure of which is most related to that of anodic oxide [7, 8], thus considered rather abnormally high. As $E_{o|e}E_{m|o}^{-1}$ rises, the peak is suppressed and, at a specific $E_{o|e}E_{m|o}^{-1}$ for each t_{an}, it vanishes. For higher $E_{o|e}E_{m|o}^{-1}$, a different plot profile appears, a minimum near the o|e interface tends to emerge, which is enhanced with rising $E_{o|e}E_{m|o}^{-1}$. The variation of E in the barrier layer thus strongly affects the shape and position of the d_c spectrum. Up to the present in the literature, the oxide density across the barrier layer was considered uniform coinciding with $d_{c,m|o}$, $d_{c,a}$, etc. Its value found by different methods varies from ≈2.8 up to 4 g cm^{-3} [5, 10, 12, 51]. The $d_{c,a}$'s found here for all t_{an}'s and $E_{o|e}E_{m|o}^{-1}$'s employed, vary from 3.21 to 3.52 g cm^{-3}, meeting these values; this constitutes a vital criterion validating the above analysis. The $d_{c,o|e}$ was 4.36–5.22 g cm^{-3} and nD_b^2 was 0.24–0.33.

Various aluminas like β-, γ-, etc. are relatively open materials. Thus, γ-Al_2O_3 is a material with high real surface area, of the order 100 m^2 g^{-1} [57], with many tetrahedral and octahedral voids [58, 59] which shows that further compressibility of γ-Al_2O_3 is possible, e.g. for thin layer material. Occurrence of electro-restriction in anodic alumina films, most related with γ-Al_2O_3 [7, 8], has been also suggested earlier [7, 22, 60–62] with compressive pressures around, e.g. 3.6×10^9 Pa [63]. Available data for compressibility of the denser and better studied a-Al_2O_3, ≈0.4×10^{-11} Pa^{-1} [64], show a volume contraction 14.4% at this pressure. Compressibility of aluminas looser than a-Al_2O_3, like β- and γ-Al_2O_3 along certain axes, can exceed that of a-Al_2O_3 even about three times [65]. Thus, the contraction of γ-Al_2O_3 under such pressures may exceed 14.4% of the volume, yielding density even >4.67 g cm^{-3}. Such values, around 4.67 g cm^{-3} depending on conditions, constitute the upper limits for material densification.

Supposedly, each plot in Fig. 8 yielding acceptable $d_{c,o|e}$ and $d_{c,a}$ could be characterised as acceptable solution. However, restrictive criteria exist defining a unique proper solution for each t_{an}, which are: (a) The change of d_c, e.g.

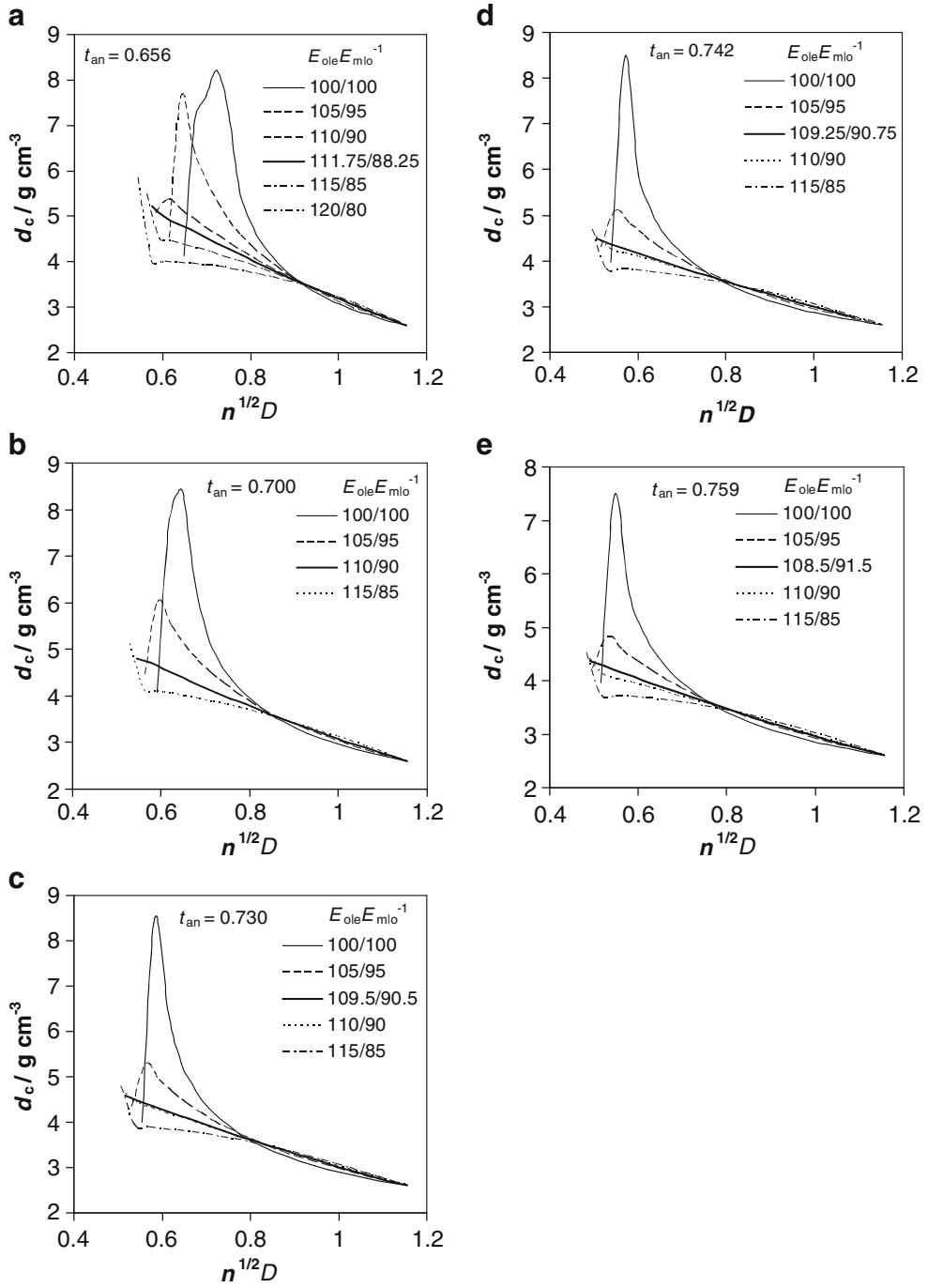

Fig. 8 Spectra of local oxide density variation across the barrier layer derived from the numerical solution of Eqs. 13, 23 and 26 at five characteristic t_{an} and various $E_{o|e}E_{m|o}^{-1}$ values. Plots in *bold* show the proper solution at different t_{an}'s approaching better reality from the ones constructed

near the interfaces, must be gradual (not abrupt and excessive) since otherwise mechanical disruption of material would occur. (b) The maximum d_c cannot exceed a value comparable to that predicted by the local compression as above. (c) The d_c must vary monotonically, as Eq. 16 anticipates, i.e. rising from the m|o to the o|e interface. Thus, the maximum d_c in the barrier layer is $d_{c,o|e}$ and the strongest electro-restriction occurs in the oxide sub-layer adjacent to the o|e interface. Figure 8 and these criteria predict that the proper/acceptable plots are those for which the peak near the o|e interface just vanishes. These plots show an almost linear variation of d_c across the barrier layer. The proper $E_{o|e}E_{m|o}^{-1}$ and $d_{c,o|e}$, $d_{c,a}$ and nD_b^2 thus determined appear in Table 2. The $d_{c,o|e}$'s in Table 2 are near the above-noted upper limit values. The $d_{c,a}$'s also fall within the range of those found in the literature by different

methods [5, 10, 12, 51] and thus they are acceptable. The drop of $d_{c,o|e}$ with t_{an}, or with rising j and falling T, shows a plausible necessity for more open material with higher vacancies concentration to allow passage of necessary ionic j. Further, more detailed search of the effect of $E_{o|e}E_{m|o}^{-1}$ values in the region near the adopted solution has no meaning since it affects $d_{c,o|e}$, $d_{c,a}$ and nD_b^2 negligibly.

The occurrence of acceptable solution for $E_{o|e}E_{m|o}^{-1} > 1$ is consistent with the fact that, due to the barrier layer geometry (Fig. 7), the true j, $j(2^{-1}\pi nD^2)^{-1}$, drops from o|e to m|o interface whilst, concurrently, d_c decreases affecting oppositely the necessary E. Their compromise yields only a slight variation of E, justifying a general tendency met in the literature to consider E as roughly constant [29, 41].

Once the $d_{c,o|e}$, $d_{c,a}$ and nD_b^2 values are known, then many other parameters can be determined. When, e.g. D_c is known, then D_b can be also calculated. As an example, the case T=25 °C, j=15 mA cm^{-2} and C_a=1.5 M is examined where t_{an}=0.742 [5]. The D_c, found from the imprints of film on the metal, is 99.4 nm which was nearly unaffected by t at $t \geq t_m$. Then, since $nD_c^2 = 4/3$ [41], n=1.35×10^{10} cm^{-2} that is acceptable. From this n and $nD_b^2 = 0.26$ (Table 2), D_b=43.9 nm and the barrier layer thickness is 27.8 nm. The corresponding ΔV_m is ≈42 V [5]. Then E_a (=anodic potential/barrier layer thickness) must be slightly lower than 1.51 V nm^{-1}. It could be considered that the above D_b value concerns only the start of steady state, i.e. near the t=t_m, and the rise of ΔV with t at t>t_m can be due to the thickening of barrier layer. However, if it were true, at the end of the process, t=120 min where ΔV ≈87 V [5], the thickness of the barrier layer would become ≈87/1.51=57.6 nm. Since D_c=99.4 nm, then D_b would become 99.4−2×57.6=−15.8 nm<0 that is unacceptable. Hence, the rise of ΔV with t must be indeed ascribed to other reasons as explained in the following. All necessary basic macroscopic, nanostructure and kinetic parameters are then available and many other important structural parameters like porosity, real surface area, specific real surface area, etc., and kinetic parameters can be also calculated, usable in many applications of porous anodic films [12, 13, 66–68].

The ratio of the volume of product oxide to the volume of consumed Al during anodising

Since Al is consumed according to Faraday's law, it is easily derived that the rate of metal thickness decrease is given by the equation:

$$k'' = \mathrm{AM}j/(3F_c d_{Al}) = z'j,\ \left(z' = 3.454 \times 10^{-5}\ \mathrm{cm^3\ C^{-1}}\right). \quad (27)$$

Therefore, the real swelling factor of oxide near the m|o interface during anodising is:

$$\mathrm{sf} = k'/k'' = (z/z')t_{an} = 1.9592t_{an} \quad (28)$$

depending exactly on the parameters affecting the transport numbers. Two other (apparent) expansion factors characterising the oxide, either during or after anodising, can also be distinguished involving (1) the volume of the whole porous film that is also k'/k'', thus coinciding with the above real sf and (2) the compact pore wall oxide thus given by $k'\left(1 - 4^{-1}\pi nD_b^2\right)/k'' = \mathrm{sf}\left(1 - 4^{-1}\pi nD_b^2\right)$. Evidently, when referring to sf, or to the, as called, Pilling–Bedworth ratio, in the case of anodic oxidation of Al, its strict meaning should be distinguished as regards the material during its growth or after its relaxation.

The mechanism of Al lattice transformation to that of anodic oxide during anodising

The almost constancy of $d_{c,m|o}$ during the Al conversion to oxide irrespective of T and j and electrolyte kind and concentration must be due to the fact that, under the high strength field action (of the order 10^7 V cm^{-1}), a transient kind lattice of virtually pure oxide is built near the m|o interface with higher spacing parameters, almost independent of the high field strength. This lattice later becomes denser as the product oxide advances towards the o|e interface (Fig. 7). The way by which this conversion can take place is given below:

The Al is crystallised in the fcc system and the cubic cell dimension is 0.4041 as found in the literature [56] or calculated from d_{Al} by the form:

$$a = \left[(\mathrm{AM}/d_{Al})(n'/N)\right]^{1/3}, \quad (29)$$

where n' is the number of atoms corresponding to each elementary cell, here n'=4. Though the transient lattice of oxide produced in the vicinity of the m|o interface is unknown, it can be considered that it comes from the fcc Al lattice by suitable removal and shift of certain Al^{3+} from the cell and entrance of corresponding O^{2-} and suitable arrangement within it and/or sharing between cells; thus, most probably, the new transient lattice also resembles cubic as regards the positions of Al^{3+} cations. The dimension of the elementary cell is:

$$a = \left[\left(\mathrm{MM}/d_{c,m/o}\right)(n'/2N)\right]^{1/3}. \quad (30)$$

From $d_{c,m|o}$=2.6023 g cm^{-3}, the cation lattice dimension is found 0.319 for c (n'=1), 0.402≈0.404 nm for bcc (n'=2) and 0.507 nm for fcc (n'=4).

The excellent agreement of Al spacing with that of bcc oxide postulates that, when the Al is transformed to oxide, each cell of Al loses five of its six Al^{3+} (half-shared with the six common face adjacent cells), presumably from five face centred sites, the sixth Al^{3+} is favoured to move to the cell space centred site and O^{2-} ions enter this Al^{3+} cation lattice and are suitably arranged within these transformed

cells and/or shared between such neighbouring cells. This is an unstable lattice existing only under the high field action. As it advances to the o|e interface, it is soon transformed to denser oxide lattice, affected by the field and the anticipated necessary local composition of oxide, demanding, on average, denser oxide towards the o|e interface or pore surface. The gradual transition of the oxide Al^{3+} cations lattice from that of Al to that of denser oxide during anodising can well explain the strong adherence of oxide to the Al surface which also persists after anodising.

Discussion

The d_c vs. D plots of the proper solutions of the model (bold plots lines in Fig. 8) show that the anodic oxide material exists under variable electro-compression/electro-restriction stresses from the o|e interface to the m|o interface during anodising. The variable compressibility of material in the space from the m|o to the o|e interface must be due to the field action and its peculiarities and is rather associated with a space charge distribution within the barrier layer, the necessary appearance of which has been discussed recently [29] though considering uniform material density, and deviation from stoichiometry during anodising. However, in view of oxide density distribution during anodising revealed in this study, strong evidences for their appearance could perhaps be given. It is obvious that further investigation is needed along the lines of this work, focussing on this specific point, to fully elucidate it.

The denser oxide layer in the pore base surface must be the reason why only a small amount of electrolyte anions is incorporated inside the barrier layer [9, 28]. Otherwise, the incorporated amount of anions could become high enough since the molar volumes of aluminium salts, like oxalate and sulphate, and those of oxide predicted by densities $d_{c,m|o}$ and $d_{c,a}$ have no noticeable differences. It is worth commenting the observed net tiny rise of t_{an} with the concentration of electrolyte anions. Their effect must be attributed to the incorporated anions. Due to the low density of oxide towards the m|o interface, the traces of incorporated anions existing in the deeper layers of the barrier layer towards the m|o interface, despite their large size, can migrate to some extent. The imperceptible rise of t_{an} with anions concentration reflects a concomitant rise of their tiny contribution to ionic conduction. Since the ionic charge transport through the barrier layer obeys virtually Faraday's law, the faint rise of t_{an} with anion concentration reflects some insignificant effect of the traces of incorporated anions near the m|o interface on parameter k (Eq. 6). As previously noted, the $C_2O_4^{2-}$ ions near the o|e interface are embodied in oxide. The amount of embodied anions, their local concentration near the o|e interface and their concentration in the bulk and pore filling solution must vary similarly. For mixtures, the bulk concentration of $C_2O_4^{2-}$ is some orders of magnitudes higher than that in pure acid electrolytes. At the same time, at constant T=25 °C and j= 15 mA cm^{-2}, for pure acid 0.5 M, t_{an}=0.730, for 1 M it is 0.733, for mixture at maximum salt concentration it is 0.739 and for acid 1.5 M (saturated solution [39]) t_{an}= 0.742 [5]. These show that the rise of t_{an} is due mainly to the rise of $C_2O_4^{2-}$ concentration in the bulk solution and thus near the o|e interface and to precipitate presence. In turn, e.g. for unsaturated solutions, these mean that a tiny error, at maximum in the third decimal figure and up to ≈0.009, or ≈1.2% (and, in extreme cases, in the second decimal figure, e.g. for $Na_2C_2O_4$ salt 0.019 or 2.6%), is made between the actual O^{2-} transport number and that found in this study. By introducing suitable k taking into consideration the contained traces of electrolyte anions, the t_{an} (referring to all migrating anions, O^{2-} and anions traces) will become closely independent of electrolyte kind and concentration. This negligible error made during t_{an} determination cannot appreciably affect the results, derived, e.g. from Fig. 6, and thus the whole above analysis is judged to be of satisfactory accuracy.

After the product material first becomes pore base wall material, e.g. around position D in Fig. 7, then it gradually moves away the region of field application as the barrier layer advances towards the Al metal through successive positions, e.g. E, F, etc. The field ceases to affect the material around D when the corresponding position of barrier layer is, e.g. F. Thus, the relaxation period of the material around D must be a time interval equal to or higher than that taken for the barrier layer to shift from D to F. The denser shell around the pore base is prone to expand and rarefy during relaxation. On the other hand, shrinkage and densification of material in cell boundaries during the above process and near the m|o after the cease of anodising and subsequent relaxation will occur. Thus, as a whole, the relaxation across the pore wall material during anodising as well as across the barrier layer after its cease must actually occur simultaneously with some material flow from the d_c maximum region towards the cell boundaries. Detectable changes in the thickness of pore wall material during relaxation are hindered by the fact that the field ceases gradually to be applied, compensating thus any proneness of material to become noticeably expanded or shrunk as a whole across the pore walls. In addition, both the material already relaxed, e.g. above D in Fig. 7, and the field below D act as a matrix sustaining the geometry and dimensions of the newly formed and sequentially relaxed material. Suggestion for some kind of oxide flow during anodising has been also made earlier [22], derived from the specific manner of shift and distortion of tungsten tracer atoms layer within the barrier layer observed after anodising.

The material during oxide growth in the barrier layer region and its relaxation as pore wall material up to some length, e.g. FD in Fig. 7, towards the pore mouths thus seems to behave like a solid-fluid material. The above relaxation process reduces, to an extent, the span of oxide density distribution across the barrier layer during anodising whilst the necessary treatment of films like washing, neutralisation, drying, etc., following anodising could even more reduce the existing local density differences and promote homogenisation. Complete homogenisation, however, is not achieved. This relaxation and homogenisation, to some extent, of material across the barrier layer and pore walls after anodising hindered the detection of striking density variations and differences until now. However, earlier results provided indications for these processes showing that, after anodising and material relaxation, the densities of O^{2-} and Al^{3+} across the barrier layer in the region adjacent to the m|o interface tend to drop towards this interface both in the initial stage before nucleation of pores and after their nucleation [4, 25]. Some slight rarefaction of a thin surface material layer compared to the immediately adjacent internal layer was also verified earlier [9] which is attributed to the removal of solvable material, e.g. Al^{3+} with embodied electrolyte anions, during treatment after anodising [40].

When the oxide fluidity during relaxation is insufficient to supply and compensate the required densification of oxide in the regions of lowest d_c that is near Al and cell boundaries FD in Fig. 7, further self-contraction of material will occur, as expected for low enough $d_{c,o|e}$ and $d_{c,a}$, or, from Table 2, at high t_{an} or at high j's and/or low enough T's (Table 1) or in conditions characterised by high enough ΔV and thus yielding thick enough barrier layer. This contraction must be strong mainly along three cell junctions surrounded in all directions by material of lowest d_c and secondly in the barrier layer near Al where the d_c distribution is radial–unidimensional and the contraction trend is weaker. These justify voids formed in such junctions of porous films grown in phosphoric acid and other electrolytes [18] having thick enough barrier layer and pore walls opposite to oxalic and sulphuric acid films showing no voids [18]. The much thicker barrier layer for the former electrolytes is easily inferred from the much higher needed ΔV to establish a given j in steady state [7, 8]. The long narrow holes crack-like voids across pore walls in films grown in the former electrolytes [18] are due to voids emerging from cell junctions above metal ridges when the average fairly strong regional contraction of oxide along pore walls enables their propagation as cracks via brittle walls. Voids can also appear in thick barrier layer in a region adjacent to Al, embracing the anion-free region, but much less frequently due, as noted, to weaker local contraction trend [18]. Voids in three cell junctions of barrier type films on preconditioned Al surface [18, 19] and their anion-free region [20] were attributed either to oxide contraction and partial crystallisation [18], oxygen inclusion [19] and to voids formed in metal ridges or voids existing in a surface layer of Al injected to oxide [20]. The absence or rarity of voids in the barrier layer of porous films, even those formed in phosphoric acid, etc. electrolytes which have thick enough barrier layer [18], may be due to that oxide thickness comparable to barrier layer thickness has many times repetitively formed and field decayed at pore bases until the establishment of steady state gradually exhausting reasons, other than the contraction of oxide during relaxation, generating voids in earlier stages.

During anodising, Al^{3+} are field ejected at pore bases [28, 41] and Al^{3+} are also added to the pore filling solution due to the chemical pore wall dissolution. As earlier noted, these Al^{3+} react with H_2O to form $Al(OH_2)_6^{3+}$ participating to processes like 3, 4 and 5 and with electrolyte anions forming aluminium oxalate which in dense solutions is condensed to colloidal aluminium oxalate precipitate [39]. The formed H^+ are much more mobile than the complex species containing Al^{3+}, from which $Al(OH)_3$ is, in addition, immobile. Thus, such complex cations and electrolyte anions, and therefore, oxalate compounds, accumulate [69]. When the ΔV vs. t plot exhibits a horizontal plateau (as predicted from Fig. 1, at low enough j's and/or high enough T's), these conditions, the higher nD_b^2 [10], and the related average total cross-section surface of pores favour the diffusion of produced species, and electrolyte anions do not notably accumulate in pores and a real steady state is established. But at high j's and low T's, these conditions, the lower nD_b^2 and the related average total cross-section surface of pores unfavour their removal. Their concentration in a thin electrolyte layer attached to pore base surface markedly rises reducing the concentration of free H_2O (the dissociative adsorption of which provides the needed oxygen for the process [40]) and raising the concentration of bulky, not mobile enough, species which favour the incorporation of electrolyte anions blocking up active lattice vacancies.

The ionic conductance inside the barrier layer anticipates migration through vacancies of mobile Al^{3+} and O^{2-} ions (counting a negligible contribution of migrating electrolyte anion traces as previously noted). For certain transport numbers of these ions, the optimum conductivity must occur for suitable intermediate bulk concentrations of mobile ions and concentration of vacancies, or in other words, around a specific d_c. Sufficient conductivity is assured when neither the bulk concentration of mobile ions and/or the bulk concentration of vacancies are low enough ($\rightarrow$0). When one of them is extremely low, i.e. when the allowable oxide density is very low or very high, the conductivity will drop thus causing a corresponding rise of

ΔV. Since the oxide is dense enough in the region of the o|e interface, the incorporation of even a small amount of electrolyte anions within the oxide blocking up such active vacancies will result in a significant drop of conductivity. The increase of the amount of incorporated anions by the above mechanism will thus cause a decrease of conductivity and rise of ΔV and E_a. It thus explains the higher E_a in the aforementioned saturated $H_2C_2O_4$ 1.5 M solution than in unsaturated anodising solutions up to ≈1.25 V nm^{-1} rising with concentration [6–8]. It is evident that, in such cases, the steady state is, strictly speaking, a quasi-steady state one. The amount and distribution of incorporated electrolyte anions in the barrier layer and, therefore, the precise way of ΔV variation with t in this stage apparently depend on all T, j, electrolyte composition and pore length or film thickness, as indeed shown in Fig. 1.

During prolonged anodising, pores open up towards their mouths, like elongated truncated cones, etc., due to the pore wall chemical dissolution [10, 36], in agreement with the negative value of parameters z_1 and z_2 [5] (Table 1). The distribution of the nature/composition of oxide across the barrier layer is extrapolated along the pore wall surface of a film with the maximum limiting h. The local rate of this process depends primarily on the local lattice rarefaction. In agreement with the rarefaction of lattice towards the m|o interface, the local rate of pore wall dissolution reaction during anodising indeed rises towards the cell boundaries [39, 40] which is thus satisfactorily explained. After anodising and film treatment, the reaction mechanism may change, mainly for unlike forming and dissolution electrolytes [21], linking other, e.g. rate controlling, factors like space charge and electronic defects, H_2 and O_2 electrochemical evolution and H^+ injection from electrolyte to the outer layer of barrier oxide [21], etc.

It has been also shown [70] that the local specific catalytic activity of oxide across the barrier layer and pore walls passes through a minimum close enough to the pore wall surface and then strongly rises towards the metal or cell boundaries. It seems that, as the oxide becomes rarer, the activity is enlarged which is well-explainable from the catalytic standpoint, whilst some effect could also be exerted from the remaining incorporated electrolyte anions. The tiny rise of activity from the minimum point to pore base surface is due to the previously noted slight opening of material caused by treatment after anodising enhanced to the surface. Since catalysis is generally very sensitive to solid catalyst structure, these show that, even after heating during catalysis experiments at 270–390 °C for some hours [70], the distribution of d_c across the barrier layer and pore walls, though suppressed, remains qualitatively similar. Complete homogenisation probably occurs only after heating above the temperature of transformation of anodic oxide to γ-Al_2O_3, e.g. 850 °C [71]. This inhomogeneity thus strongly differs from that of barrier layer of porous film freshly formed in phosphoric acid concerning immobile space charge and electronic defects which is cancelled after annealing at 200 °C [21]. Suitable removal of the denser and more contaminated layer of pore wall surface, leaving only the rarer and purer oxide near cell boundaries of roughly cylindrical pores is expected to reveal a catalytically ultra-active material. This can be also achieved by choosing conditions yielding large n and D_b and lower $d_{c,a}$. All these will result in the enlargement of the geometric surface of pores, of specific real surface and of the adsorptive and catalytically active one on the pore surface. Overall, the elucidation of the mechanism of film growth during the process achieved in this study allows the design of peculiar properties of material required for both the aforementioned and newly conceived applications.

The denser pore wall and pore base surface sub-layer during anodising must have higher mechanical strength. This layer and the shell of purer and rarer oxide near the m|o interface under different electro-restriction stresses must play a crucial role in self-organising of structure already established during the start of steady state [5] (BC in Fig. 1). The first plays the role of a frame for sustaining the columnar cellular structure and the second the mean for correcting faults and change of developing structure by setting homogeneous distributions along the Al surface through pushing stresses between each triad, usually, or quadruplet, rarely, of touching units of barrier layer and pore wall around pore bases.

Conclusions

1. The t_{an} and t_{ca} depend practically solely on T and j. The electrolyte anions seemingly exert a negligible effect on t_{an} and t_{ca} through their traces embodied in deeper layer of barrier layer near the m|o interface. They do not depend on the kind and concentration of electrolyte cation. The rate of film thickness growth is proportional to the partial anionic O^{2-} current, jt_{an}.
2. By a numerical solution of developed model, it was found that the density of oxide during the film growth changes across the barrier layer. It is constant, independent of conditions, in the vicinity of m|o, ≈2.6 g cm^{-3}, and rises towards the o|e interface where it becomes maximum, 4.36–5.22 g cm^{-3}. This spectrum of oxide density appears as a result of electrical field peculiarities yielding variable electro-restriction stresses from the m|o to the o|e interface. The E varies relatively slightly from the o|e to the m|o interface whilst $E_{o|e}/E_{m|o}$ slightly decreases with t_{an}. The mean density value across the barrier layer generally lies within ≈3.21–

3.52 g cm^{-3} close to values determined by entirely different experimental methods.

3. The mechanism of Al transformation to oxide in the m|o interface during anodising embraces the transformation of metal lattice to a transient lattice of oxide, existing under the field action with cation lattice spacing common with that of metal that becomes denser as the oxide product near the m|o is shifted towards the o|e interface and becomes the wall material towards the pore surface. The model, and related whole method, also allows the determination of many structural and kinetic features. Many peculiar properties of porous anodic alumina films are satisfactorily explained by the local density distribution and mechanism of Al transformation to oxide.
4. The present results and relevant analysis extensively change our heretofore mind on the kinetics and mechanism of growth of porous anodic films, their structure and nature/composition during anodising of Al, assisting in the better comprehension of the relevant solid-state electrochemistry. Considerable consequences in a large number of their scientific and technological applications and new applications can thus be conceived. Design and optimising of their structure and particular properties are now possible which are of great importance for their numerous applications.

References

1. Surganov VF, Gorokh GG (1993) Mater Lett 17:121. doi:10.1016/0167-577X(93)90069-A
2. Surganov V, Janson C, Nielsen JCG, Morgen P, Gorokh G, Larsen AN (1988) Electrochim Acta 33:517. doi:10.1016/0013-4686(88)80169-5
3. Dell'Oca CJ, Fleming PJ (1976) J Electrochem Soc 123:1487. doi:10.1149/1.2132624
4. Parkhutik VP (1986) Corros Sci 26:295. doi:10.1016/0010-938X(86)90050-8
5. Patermarakis G, Chandrinos J, Masavetas K (2007) J Solid State Electrochem 11:1191. doi:10.1007/s10008-006-0259-z
6. Keller F, Hunter MS, Robinson DL (1953) J Electrochem Soc 100:411. doi:10.1149/1.2781142
7. Diggle JW, Downie TC, Goulding CW (1969) Chem Rev 69:365. doi:10.1021/cr60259a005
8. Young L (1961) Anodic oxide films. Academic, London
9. Thompson GE, Furneaux RC, Wood GC (1978) Corros Sci 18:481. doi:10.1016/S0010-938X(78)80041-9
10. Patermarakis G, Lenas P, Karavassilis C, Papayiannis G (1991) Electrochim Acta 36:709. doi:10.1016/0013-4686(91)85162-Z
11. Patermarakis G, Kerassovitou P (1992) Electrochim Acta 37:125. doi:10.1016/0013-4686(92)80021-D
12. Martin CR (1996) Chem Mater 8:1739. doi:10.1021/cm960166s
13. Kovtyukhova N, Mallouk TE (2005) Adv Mater 17:187. doi:10.1002/adma.200400874
14. Jessensky O, Müller F, Gösele U (1998) Appl Phys Lett 72 (10):1173. doi:10.1063/1.121004
15. Zhang L, Cho HS, Li F, Metzger RM, Doyle WD (1998) J Mater Sci Lett 17:291. doi:10.1023/A:1006577504924
16. Jessensky O, Müller F, Gösele U (1998) J Electrochem Soc 145:3735. doi:10.1149/1.1838867
17. Nielsch K, Choi J, Schwirn K, Wehrspohn RB, Gösele U (2002) Nano Lett 2(7):677. doi:10.1021/nl025537k
18. Ono S, Ichinose H, Masuko N (1991) J Electrochem Soc 138:3705. doi:10.1149/1.2085484
19. Ono S, Ichinose H, Masuko N (1992) J Electrochem Soc 139:L81. doi:10.1149/1.2221289
20. Huang R, Hebert KR, Chumbley LS (2004) J Electrochem Soc 151(7):B379. doi:10.1149/1.1753582
21. Vrublevsky I, Parkoun V, Schreckenbach J, Goebel Werner A (2006) Appl Surf Sci 252:5100. doi:10.1016/j.apsusc.2005.07.028
22. Garcia-Vergara SJ, Skeldon P, Thompson GE, Habazaki H (2005) Electrochim Acta 52:681. doi:10.1016/j.electacta.2006.05.054
23. Xu Y, Thompson GE, Wood GC, Bethune B (1987) Electrochim Acta 27:83
24. Lanford WA, Alwitt RS, Dyer CK (1980) J Electrochem Soc 127:405. doi:10.1149/1.2129679
25. Patermarakis G, Kytopoulos V (2007) Mater Lett 61:4997. doi:10.1016/j.matlet.2007.03.091
26. Shimizu K, Brown GM, Habazaki H, Kobayashi K, Skeldon P, Thompson GE, Wood GC (1999) Electrochim Acta 44:2297. doi:10.1016/S0013-4686(98)00355-7
27. Shimizu K, Habazaki H, Skeldon P, Thompson GE, Wood GC (2001) Electrochim Acta 46:4379. doi:10.1016/S0013-4686(01)00660-0
28. Thompson GE (1997) Thin Solid Films 297:192. doi:10.1016/S0040-6090(96)09440-0
29. Houser JE, Heber KR (2006) J Electrochem Soc 153:B566. doi:10.1149/1.2360763
30. Houser JE, Hebert KR (2008) Phys Status Solidi A 205:2396. doi:10.1002/pssa.200779407
31. Sui YC, Cui BZ, Martínez L, Perez R, Sellmyer DJ (2002) Thin Solid Films 406:64. doi:10.1016/S0040-6090(01)01769-2
32. Dodos D (1975) Electrochemical data. Elsevier, Budapest
33. Vogel AI (1976) Macro and semimicro quantitative analysis. Longman, London
34. Alexeyev VN (1980) Qualitative chemical analysis. Mir, Moscow
35. Patermarakis G (2006) J Solid State Electrochem 10:211. doi:10.1007/s10008-005-0665-7
36. Patermarakis G, Tzouvelekis D (1994) Electrochim Acta 39:2419. doi:10.1016/0013-4686(94)00203-7
37. Patermarakis G, Moussoutzanis K (2001) Corros Sci 43:1433. doi:10.1016/S0010-938X(00)00161-X
38. Patermarakis G, Moussoutzanis K (2002) Corros Sci 44:1433. doi:10.1016/S0010-938X(01)00180-9
39. Patermarakis G, Masavetas K (2006) J Electroanal Chem 588:179. doi:10.1016/j.jelechem.2005.12.021
40. Patermarakis G, Moussoutzanis K, Chandrinos J (2001) J Solid State Electrochem 6:39. doi:10.1007/s100080000176
41. Patermarakis G, Moussoutzanis K (1995) Electrochim Acta 40:699. doi:10.1016/0013-4686(94)00347-4
42. Li AP, Müller F, Birner A, Nielsch K, Gösele U (1997) J Appl Phys 84(11):6023. doi:10.1063/1.368911
43. Li AP, Müller F, Gösele U (2000) Electrochem Solid-State Lett 3 (3):131. doi:10.1149/1.1390979
44. Masuda H, Yotsuya M, Asano M, Nishio K, Nakao M, Yokoo A, Tamamura T (2001) Appl Phys Lett 78(6):826. doi:10.1063/1.1344575
45. Pan H, Lin J, Feng Y, Gao H (2005) IEEE Transactions on Nanotechnology 3:462. doi:10.1109/TNANO.2004.834187
46. Patermarakis G, Chandrinos J, Moussoutzanis K (2001) J Electroanal Chem 510:59. doi:10.1016/S0022-0728(01)00544-7

47. Belca I, Kasalica B, Zekovic L, Jovanic B, Vasilic R (1999) Electrochim Acta 45:993. doi:10.1016/S0013-4686(99)00284-4
48. Kittel C (1968) Introduction to solid state physics, 3rd edn. Wiley, New York
49. Yamamoto Y, Baba N (1983) Thin Solid Films 101:329. doi:10.1016/0040-6090(83)90099-8
50. Takahashi H, Fujimoto K, Nagayama M (1988) J Electrochem Soc 135:1349. doi:10.1149/1.2095981
51. Thompson GE, Wood GC, Shimizu K (1981) Electrochim Acta 26:951. doi:10.1016/0013-4686(81)85060-8
52. Xu Y, Thompson GE, Wood GC (1983) J Electrochem Soc 130:2395. doi:10.1149/1.2119596
53. Thompson GE, Xu Y, Skeldon P, Shimizu K, Han SH, Wood GC (1978) Philos Mag B 55:651. doi:10.1080/13642818708218371
54. O'Sullivan JP, Wood GC (1970) Proc R Soc Lond A Math Phys Sci 317:511. doi:10.1098/rspa.1970.0129
55. Nagayama M, Tamura K, Takahashi H (1970) Corros Sci 10:617. doi:10.1016/S0010-938X(70)80055-5
56. Weast RC (ed) (1980) Handbook of chemistry and physics, 60th edn. CRC, Boca Raton, p B-52
57. Patermarakis G (2003) Appl Catal A Gen 252:231. doi:10.1016/S0926-860X(03)00411-3
58. Mo SD, Xu YN, Ching WY (1997) J Am Ceram Soc 80:1193
59. McHale JM, Navrotsky A, Perrota AJ (1997) J Phys Chem 101:603
60. Sato N (1971) Electrochim Acta 16:1683. doi:10.1016/0013-4686(71)85079-X
61. Skeldon P, Thompson GE, Wood GC, Zhou X, Habazaki H, Shimizu K (1997) Philos Mag A 76:729. doi:10.1080/01418619708214206
62. Zhou X, Thompson GE, Paez MA, Skeldon P, Habazaki H, Shimizu K, Wood GC (2000) J Electrochem Soc 147:1747. doi:10.1149/1.1393428
63. Bradhurst DH, Leach JSL (1966) J Eelectrochem Soc 113:1245. doi:10.1149/1.2423797
64. Samsonov GV (1973) The oxide handbook. IFI/Plenum, New York
65. Arashi H, Naito H, Kaimai A (1993) Mater Sci 28:5727
66. Patermarakis G, Moussoutzanis K, Chandrinos J (1999) Appl Catal A Gen 180:345. doi:10.1016/S0926-860X(98)00356-1
67. Patermarakis G, Nikolopoulos N (1999) J Catal 187:311. doi:10.1006/jcat.1999.2627
68. Ganley JC, Riechmann KL, Seebauer EG (2004) J Catal 227 (1):26. doi:10.1016/j.jcat.2004.06.016
69. Patermarakis G (1998) J Electroanal Chem 447:25. doi:10.1016/S0022-0728(97)00604-9
70. Patermarakis G, Moussoutzanis K, Nicolopoulos N (1999) J Solid State Electrochem 3:193. doi:10.1007/s100080050147
71. Ruckenstein E, Chu YF (1979) J Catal 52:109. doi:10.1016/S0021-9517(79)80049-4